Appl. Math. Mech. -Engl. Ed., **41**(5), 741–752 (2020)

Applied Mathematics and Mechanics (English Edition)

https://doi.org/10.1007/s10483-020-2608-9

Darcy-Forchheimer flow by rotating disk with partial slip*

T. HAYAT[1,2], F. HAIDER[1,†], T. MUHAMMAD[1], A. ALSAEDI[2]

1. Department of Mathematics, Quaid-i-Azam University, Islamabad 44000, Pakistan;
2. Nonlinear Analysis and Applied Mathematics (NAAM) Research Group, Department of Mathematics, Faculty of Science, King Abdulaziz University, Jeddah 21589, Saudi Arabia

(Received Jan. 14, 2020 / Revised Feb. 24, 2020)

Abstract The viscous dissipation and heat transfer in the Darcy-Forchheimer flow by a rotating disk are examined. The partial slip conditions are invoked. The optimal series solutions are computed via the optimal homotopic analysis method (OHAM). The thermophoresis and Brownian motions are studied. The Darcy-Forchheimer relation characterizes the porous space. The roles of influential variables on the physical quantities are graphically examined. A reduction in the local Nusselt number is observed through thermophoresis and thermal slip parameters. The local Sherwood number depicts an increasing trend for the higher Brownian motion and concentration slip parameters.

Key words Darcy-Forchheimer flow, nanofluid, viscous dissipation, slip condition, optimal homotopy analysis method (OHAM)

Chinese Library Classification O357
2010 Mathematics Subject Classification 76S05

Nomenclature

u, v, w,	velocity components;	L_1,	velocity slip parameter;
$\nu_{\rm nf}$,	kinematic nanofluid viscosity;	L_2,	thermal slip parameter;
r, φ, z,	polar coordinates;	L_3,	concentration slip parameter;
K^*,	permeability of porous space;	$T_{\rm w}$,	surface temperature;
$\mu_{\rm f}$,	dynamic viscosity of fluid;	$C_{\rm w}$,	surface concentration;
$\nu_{\rm f}$,	kinematic viscosity of fluid;	T_∞,	ambient temperature;
$\rho_{\rm f}$,	density of base fluid;	C_∞,	ambient concentration;
$\alpha_{\rm m}$,	thermal diffusivity;	λ,	local porosity parameter;
$C_{\rm b}^*$,	drag coefficient;	F_r,	Forchheimer number;
F,	non-uniform inertia coefficient;	$N_{\rm t}$,	thermophoresis parameter;
$\rho_{\rm nf}$,	nanofluid density;	Sc,	Schmidt number;
$D_{\rm B}$,	Brownian diffusion;	γ_1,	dimensionless velocity slip parameter;
$(\rho c_p)_{\rm f}$,	specific heat capacity of base fluid;	Pr,	Prandtl number;
$D_{\rm T}$,	thermophoresis diffusion;	$N_{\rm b}$,	Brownian motion parameter;
Ω,	angular frequency;	Ec,	Eckert number;

* Citation: HAYAT, T., HAIDER, F., MUHAMMAD, T., and ALSAEDI, A. Darcy-Forchheimer flow by rotating disk with partial slip. *Applied Mathematics and Mechanics* (*English Edition*), **41**(5), 741–752 (2020) https://doi.org/10.1007/s10483-020-2608-9

† Corresponding author, E-mail: farwahaider@math.qau.edu.pk

Re_r,	local Reynolds number;	C_f, C_g,	skin friction coefficients;
γ_2,	dimensionless thermal slip parameter;	θ,	dimensionless temperature;
f', g,	dimensionless velocities;	Sh,	Sherwood number;
γ_3,	dimensionless concentration slip parameter;	ϕ,	dimensionless concentration;
Nu,	local Nusselt number;	ζ,	dimensionless parameter.

1 Introduction

Nanoparticles are dilute suspensions of ultrafine particles in conventional base liquids. Due to their nanometer size and large surface area, nanoparticles have exceptional physical and chemical properties. They are widely used in industrial and biomedical applications. Applications of nanoparticles in biomedical industry include probing of DNA structure, detection of proteins, fluorescent biological labels, tumor destruction via heating (hyperthermia), and purification and separation of biological molecules and cells. The pioneering work on nanofluids was done by Choi[1], who observed that thermal conductivities and heat transfer of such fluids can be enhanced by the infusion of metallic nanoparticles in base liquids. Eastman et al.[2] analyzed the thermal conductivity enhancement in ethylene glycol in presence of copper nanoscale sized particles. It was noted that the particle size does not affect the thermal conductivity of nanofluid. To study convective transport of nanofluids, a model was recommended by Buongiorno[3]. It was noticed that there are seven slip mechanisms among which the Brownian diffusion and thermophoresis are most significant. Tiwari and Das[4] interpreted the heat transfer enhancement of nanofluids in a heated square cavity. Abu-Nada and Oztop[5] considered a natural convective flow in an enclosure filled with the Cu-water nanofluid. Hsiao[6] explored the effects of radiation and conjugate mixed convection in the flow of nanofluids. A partial slip in the stagnation point flow of nanofluids with mixed convection was illustrated by Hsiao[7]. A few attempts about nanofluid flow problems were reviewed in Refs. [8]–[17].

Fluid transport in composite systems composed of spaces filled with a fluid plays a significant role in various scientific and industrial fields, such as contaminant pollution control, underground spreading of waste substance, hydrocarbon exploitation, nuclear waste document, water resource management, hazardous waste isolation, and sustainable urban drainage. Darcy's law is inadequate for the porous space with a large pore radius. Hence, a nonlinear term was introduced by Forchheimer[18] in the momentum equation. Muskat[19] concluded its validity for high Reynolds numbers. The dissipative flow of nanofluids through a porous space was scrutinized by Seddeek[20]. Sadiq and Hayat[21] studied the convective flow of Maxwell fluids saturating a Darcy-Forchheimer porous space. A few developments in this direction can be consulted via the attempts in Refs. [22]–[29].

The flow by a rotating disk has a key role in many industrial parts including shrink fits, flywheels, gears, and rotors. Rotating disks are useful in thermal power generating systems, rotor-stator spinning disc reactors, electric-power generation, brake systems, rotating sawing machines, and rotational air cleaners. A similarity analysis of the laminar flow was presented by von Kármán[30]. Thermal and mass transfer analysis of the flow over a rough rotating porous disk was interpreted by Turkyilmazoglu and Senel[31]. An entropy generation analysis of the partial slip flow by a porous rotating disk with variable properties was elucidated by Rashidi et al.[32]. The flow of nanofluids by a rotating disk was examined by Turkyilmazoglu[33]. Hatami et al.[34] explored effects of disk contracting, rotation, and heat transfer. Solution development is due to the least square method. Mustafa et al.[35] interpreted the flow of nanofluids by a stationary disk subject to a rotating frame. Sheikholeslami et al.[36] developed numerical solutions for nanofluid spraying due to an inclined rotating disk. Transient thermophoretic particle deposition for the forced convective flow of micropolar fluid by a rotating disk was studied by Doh and Muthtamilselvan[37]. The flow of suspension of gyrotactic microorganism

and nanoparticles with thermal radiation past a variable thick rotating disk was elucidated by Qayyum et al.[38]. The unsteady flow of nanofluids by a generalized hybrid model between two rotating disks was elaborated by Xu[39]. Majeed et al.[40] provided the heat transfer analysis of a viscous fluid in permeable media.

The present paper intends to describe the slip flow of nanofluids by a rotating disk using the Buongiorno model. Random movement and thermophoretic diffusion processes are examined. Viscous dissipation is accounted. The optimal homotopy analysis method (OHAM)[41–50] is employed for solutions to the governing nonlinear system. Graphical results are achieved by considering important variables.

2 Problem development

A three-dimensional (3D) steady flow of nanofluids through a porous space is considered. The rotating disk at $z=0$ generates the flow. The partial slip conditions of the velocity, the temperature, and the concentration are employed. Viscous dissipation, Brownian motion, and thermophoresis are also considered. The disk rotates with a constant angular velocity Ω. Here, u, v, and w depict the velocity components along the r-, φ-, and z-directions, respectively. The relevant equations for the 3D flow are

$$\frac{\partial u}{\partial r}+\frac{u}{r}+\frac{\partial w}{\partial z}=0, \tag{1}$$

$$u\frac{\partial u}{\partial r}-\frac{v^2}{r}+w\frac{\partial u}{\partial z}=\nu_{\rm nf}\Big(\frac{\partial^2 u}{\partial r^2}+\frac{1}{r}\frac{\partial u}{\partial r}-\frac{u}{r^2}+\frac{\partial^2 u}{\partial z^2}\Big)-\frac{\nu_{\rm nf}}{K^*}u-Fu^2, \tag{2}$$

$$u\frac{\partial v}{\partial r}+\frac{uv}{r}+w\frac{\partial v}{\partial z}=\nu_{\rm nf}\Big(\frac{\partial^2 v}{\partial r^2}+\frac{1}{r}\frac{\partial v}{\partial r}-\frac{v}{r^2}+\frac{\partial^2 v}{\partial z^2}\Big)-\frac{\nu_{\rm nf}}{K^*}v-Fv^2, \tag{3}$$

$$u\frac{\partial w}{\partial r}+w\frac{\partial w}{\partial z}=\nu_{\rm nf}\Big(\frac{\partial^2 w}{\partial r^2}+\frac{1}{r}\frac{\partial w}{\partial r}+\frac{\partial^2 w}{\partial z^2}\Big)-\frac{\nu_{\rm nf}}{K^*}w-Fw^2, \tag{4}$$

$$\begin{aligned}u\frac{\partial T}{\partial r}+w\frac{\partial T}{\partial z}=\alpha_{\rm m}\Big(\frac{\partial^2 T}{\partial r^2}+\frac{1}{r}\frac{\partial T}{\partial r}+\frac{\partial^2 T}{\partial z^2}\Big)+\frac{\rho c}{(\rho c_p)_{\rm f}}\Big(D_{\rm B}\Big(\frac{\partial T}{\partial r}\frac{\partial C}{\partial r}+\frac{\partial T}{\partial z}\frac{\partial C}{\partial z}\Big)\\ +\frac{D_{\rm T}}{T_\infty}\Big(\Big(\frac{\partial T}{\partial r}\Big)^2+\Big(\frac{\partial T}{\partial z}\Big)^2\Big)\Big)-\frac{\mu}{\rho c_p}\Big(2\Big(\Big(\frac{\partial u}{\partial r}\Big)^2+\Big(\frac{u}{r}\Big)^2+\Big(\frac{\partial w}{\partial z}\Big)^2\Big)\\ +\Big(\frac{\partial v}{\partial r}-\frac{v}{r}\Big)^2+\Big(\frac{\partial v}{\partial z}\Big)^2+\Big(\frac{\partial u}{\partial z}+\frac{\partial w}{\partial r}\Big)^2\Big),\end{aligned} \tag{5}$$

$$u\frac{\partial C}{\partial r}+w\frac{\partial C}{\partial z}=D_{\rm B}\Big(\frac{\partial^2 C}{\partial r^2}+\frac{1}{r}\frac{\partial C}{\partial r}+\frac{\partial^2 C}{\partial z^2}\Big)+\frac{D_{\rm T}}{T_\infty}\Big(\frac{\partial^2 T}{\partial r^2}+\frac{1}{r}\frac{\partial T}{\partial r}+\frac{\partial^2 T}{\partial z^2}\Big), \tag{6}$$

$$\begin{cases}u=L_1\dfrac{\partial u}{\partial z},\quad v=r\Omega+L_1\dfrac{\partial v}{\partial z},\quad w=0,\quad T=T_{\rm w}+L_2\dfrac{\partial T}{\partial z},\quad C=C_{\rm w}+L_2\dfrac{\partial C}{\partial z}\quad \text{at}\quad z=0,\\ u\to 0,\quad v\to 0,\quad T\to T_\infty,\quad C\to C_\infty\quad \text{as}\quad z\to\infty,\end{cases} \tag{7}$$

in which $F=\frac{C_{\rm b}^*}{K^{*1/2}}$ is the non-uniform inertia coefficient of the porous medium, K^* is the permeability of the porous space, $C_{\rm b}^*$ is the drag coefficient, and L_1, L_2, and L_3 are the velocity, thermal, and concentration slip coefficients, respectively. Consider

$$\begin{cases}u=r\Omega f'(\zeta),\quad v=r\Omega g(\zeta),\quad w=-\sqrt{2\Omega\nu}f(\zeta),\\ \theta(\zeta)=\dfrac{T-T_\infty}{T_{\rm w}-T_\infty},\quad \phi(\zeta)=\dfrac{C-C_\infty}{C_{\rm w}-C_\infty},\quad \zeta=\Big(\dfrac{2\Omega}{\nu}\Big)^{1/2}z,\end{cases} \tag{8}$$

where ν represents the kinematic viscosity.

An incompressibility condition is trivially justified, and Eqs. (2)–(8) become

$$2f''' - \lambda f' + 2ff'' - f'^2 + g^2 - F_r f'^2 = 0, \tag{9}$$

$$2g'' - g + 2fg' - 2f'g - F_r g^2 = 0, \tag{10}$$

$$\frac{1}{Pr}\theta'' + f\theta' + N_{\mathrm{b}}\theta'\phi' + N_{\mathrm{t}}\theta'^2 + Ec\Big(\frac{1}{Re_r}3f'^2 + g'^2 + f''^2\Big) = 0, \tag{11}$$

$$\frac{1}{Sc}\phi'' + f\phi' + \frac{N_{\mathrm{t}}}{N_{\mathrm{b}}}\frac{1}{Sc}\theta'' = 0, \tag{12}$$

$$\begin{cases} f = 0, \quad f' = \gamma_1 f'', \quad g = 1 + \gamma_1 g', \quad \theta = 1 + \gamma_2\theta', \quad \phi = 1 + \gamma_3\phi' \quad \text{at} \quad \zeta = 0, \\ f' \to 0, \quad g \to 0, \quad \theta \to 0, \quad \phi \to 0 \quad \text{as} \quad \zeta \to \infty, \end{cases} \tag{13}$$

where γ_1, γ_2, and γ_3 stand for the velocity, thermal, and concentration slip parameters, F_r stands for the Forchheimer number, Ec stands for the Eckert number, λ stands for the local porosity parameter, N_{b} stands for the Brownian motion parameter, Sc stands for the Schmidt number, N_{t} stands for the thermophoresis parameter, and Pr stands for the Prandtl number. We set these definitions as

$$\begin{cases} \gamma_1 = L_1\sqrt{\dfrac{2\Omega}{\nu}}, \quad \gamma_2 = L_2\sqrt{\dfrac{2\Omega}{\nu}}, \quad \gamma_3 = L_3\sqrt{\dfrac{2\Omega}{\nu}}, \quad F_r = \dfrac{C_{\mathrm{b}}^*}{K^{*1/2}}r, \quad \lambda = \dfrac{\nu}{\Omega K}, \\ N_{\mathrm{b}} = \dfrac{(\rho c_p)D_{\mathrm{T}}(T_{\mathrm{w}} - T_\infty)}{(\rho c_p)_{\mathrm{f}}T_\infty\nu}, \quad N_{\mathrm{t}} = \dfrac{(\rho c_p)D_{\mathrm{B}}(C_{\mathrm{w}} - C_\infty)}{(\rho c_p)_{\mathrm{f}}\nu}, \quad Ec = \dfrac{(r\Omega)^2}{(T_{\mathrm{w}} - T_\infty)\,c_p}, \\ Pr = \dfrac{\nu_{\mathrm{f}}}{\alpha_{\mathrm{m}}}, \quad Sc = \dfrac{\nu}{D_{\mathrm{B}}}. \end{cases} \tag{14}$$

The expressions of the skin friction coefficients and the local Nusselt and Sherwood numbers satisfy

$$\begin{cases} (Re_r)^{1/2}C_f = f''(0), \\ (Re_r)^{1/2}C_g = g'(0), \\ (Re_r)^{-1/2}Nu = -\theta'(0), \\ (Re_r)^{-1/2}Sh = -\phi'(0). \end{cases} \tag{15}$$

Here, $Re_r = \frac{(\Omega r)\,r}{2\nu}$ depicts the local Reynolds number.

3 OHAM solutions

It is noted that Eqs. (9)–(12) represent the system of nonlinear equations. The optimal series arrangement of the system of nonlinear problem is done by the OHAM. The initial deformations and auxiliary linear operators are

$$f_0(\zeta) = 0, \quad g_0(\zeta) = \frac{1}{1+\gamma_1}\mathrm{e}^{-\zeta}, \quad \theta_0(\zeta) = \frac{1}{1+\gamma_2}\mathrm{e}^{-\zeta}, \quad \phi_0(\zeta) = \frac{1}{1+\gamma_3}\mathrm{e}^{-\zeta}, \tag{16}$$

$$L_f = \frac{\mathrm{d}^3 f}{\mathrm{d}\zeta^3} - \frac{\mathrm{d}f}{\mathrm{d}\zeta}, \quad L_g = \frac{\mathrm{d}^2 g}{\mathrm{d}\zeta^2} - g, \quad L_\theta = \frac{\mathrm{d}^2\theta}{\mathrm{d}\zeta^2} - \theta, \quad L_\phi = \frac{\mathrm{d}^2\phi}{\mathrm{d}\zeta^2} - \phi \tag{17}$$

with

$$\begin{cases} L_f(\widetilde{P}_1^{**} + \widetilde{P}_2^{**}\mathrm{e}^{\zeta} + \widetilde{P}_3^{**}\mathrm{e}^{-\zeta}) = 0, \quad L_g(\widetilde{P}_4^{**}\mathrm{e}^{\zeta} + \widetilde{P}_5^{**}\mathrm{e}^{-\zeta}) = 0, \\ L_\theta(\widetilde{P}_6^{**}\mathrm{e}^{\zeta} + \widetilde{P}_7^{**}\mathrm{e}^{-\zeta}) = 0, \quad L_\phi(\widetilde{P}_8^{**}\mathrm{e}^{\zeta} + \widetilde{P}_9^{**}\mathrm{e}^{-\zeta}) = 0. \end{cases} \tag{18}$$

Here, $\widetilde{P}_j^{**}$ $(j = 1, 2, \cdots, 9)$ are arbitrary constants.

4 Solution convergence

BVPh 2.0 is employed for the solutions. These solution expressions contain h_f, h_g, h_θ, and h_ϕ which have a vital role in homotopic solutions. We can determine the optimal data of h_f, h_g, h_θ, and h_ϕ by taking the minimum error. In order to save the CPU time, the average squared residual error is utilized at the mth-order of deformation, i.e.,

$$\varepsilon_m^f = \frac{1}{k+1}\sum_{j=0}^{k}\Big(N_f\Big(\sum_{i=0}^{m}\hat{f}(\zeta), \sum_{i=0}^{m}\hat{g}(\zeta)\Big)_{\zeta=j\delta\zeta}\Big)^2, \tag{19}$$

$$\varepsilon_m^g = \frac{1}{k+1}\sum_{j=0}^{k}\Big(N_g\Big(\sum_{i=0}^{m}\hat{f}(\zeta), \sum_{i=0}^{m}\hat{g}(\zeta)\Big)_{\zeta=j\delta\zeta}\Big)^2, \tag{20}$$

$$\varepsilon_m^\theta = \frac{1}{k+1}\sum_{j=0}^{k}\Big(N_\theta\Big(\sum_{i=0}^{m}\hat{f}(\zeta), \sum_{i=0}^{m}\hat{g}(\zeta), \sum_{i=0}^{m}\hat{\theta}(\zeta)\Big)_{\zeta=j\delta\zeta}\Big)^2, \tag{21}$$

$$\varepsilon_m^\phi = \frac{1}{k+1}\sum_{j=0}^{k}\Big(N_\phi\Big(\sum_{i=0}^{m}\hat{f}(\zeta), \sum_{i=0}^{m}\hat{\theta}(\zeta), \sum_{i=0}^{m}\hat{\phi}(\zeta)\Big)_{\zeta=j\delta\zeta}\Big)^2, \tag{22}$$

where h_f, h_g, h_θ, and h_ϕ represent nonlinear operators for Eqs. (9)–(12), respectively.

Following Liao[41], we have

$$\varepsilon_m^{\mathrm{t}} = \varepsilon_m^f + \varepsilon_m^g + \varepsilon_m^\theta + \varepsilon_m^\phi, \tag{23}$$

where $\varepsilon_m^{\mathrm{t}}$ is the total squared residual error, $\delta\zeta = 0.5$, and $k = 20$. At the 2nd-order of deformations, the optimal data of convergence control parameters are $h_f = -0.820\,207, h_g = -0.702\,691$, $h_\theta = 1.122\,31$, and $h_\phi = -0.962\,981$. The total averaged squared residual error is $\varepsilon_m^{\mathrm{t}} = 3.11\times10^{-2}$. A sketch for the total residual error is portrayed in Fig. 1. By considering the optimal data of convergence control variables, the individual average squared residual errors at $m = 2$ are interpreted in Table 1. It is analyzed that the average squared residual error reduces for higher-order deformations.

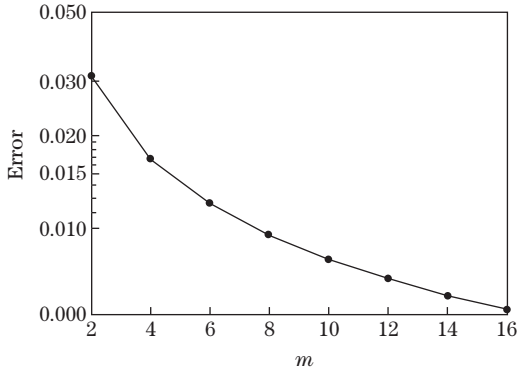

Fig. 1 Sketch for total residual error

Table 1 Optimal convergence control variables and total average squared residual errors[25]

m	ε_m^f	ε_m^g	ε_m^θ	ε_m^ϕ
2	1.11×10^{-3}	5.71×10^{-3}	1.05×10^{-2}	1.38×10^{-2}
6	3.11×10^{-4}	1.43×10^{-3}	4.51×10^{-3}	5.79×10^{-3}
10	1.63×10^{-4}	7.17×10^{-4}	3.01×10^{-3}	4.04×10^{-3}
14	1.04×10^{-4}	4.53×10^{-4}	2.30×10^{-3}	3.21×10^{-3}
16	8.70×10^{-5}	3.77×10^{-4}	2.07×10^{-3}	2.93×10^{-3}

5 Discussion

The main interest in this section is to analyze the thermal $\theta(\zeta)$ and concentration $\phi(\zeta)$ fields for the flow variables such as the Eckert number Ec, the Brownian motion parameter $N_{\rm b}$, the local Reynolds number Re_r, the Prandtl number Pr, the velocity, the thermal and concentration slip parameters γ_1, γ_2, and γ_3, the Schmidt number Sc, and the thermophoresis parameter $N_{\rm t}$. Figure 2 is interpreted for the impact of $N_{\rm b}$ on the temperature field $\theta(\zeta)$. A higher estimation of $N_{\rm b}$ shows more Brownian diffusion within the particles at lower viscous forces which enhances the thermal field $\theta(\zeta)$. Figure 3 characterizes the consequences of $N_{\rm t}$ on $\theta(\zeta)$. A higher $N_{\rm t}$ yields a stronger temperature field $\theta(\zeta)$. Physically, thermophoresis refers to the behavior of small particles within the fluid in the direction of decreasing temperature. The particles move away from the hot source to the cold regime which results in an enhancement of the thermal field $\theta(\zeta)$. An increase in the Eckert number Ec leads to an increase in $\theta(\zeta)$ (see Fig. 4). The temperature distribution $\theta(\zeta)$ for varying local Reynolds numbers Re_r is portrayed in Fig. 5. It is analyzed that a larger Re_r leads to a higher $\theta(\zeta)$. Figure 6 shows the variations of the Prandtl number Pr on the temperature $\theta(\zeta)$. A higher estimation of Pr yields a lower temperature $\theta(\zeta)$ and a smaller associated layer thickness. Here, $\theta(\zeta)$ is reduced via the thermal slip parameter γ_2 due to a decrease in heat transfer from the surface towards the adjacent layers of the fluid (see Fig. 7). The effect of $N_{\rm b}$ on the concentration $\phi(\zeta)$ is depicted in Fig. 8. Clearly, $\phi(\zeta)$ and the related layer thickness reduce for $N_{\rm b}$. Figure 9 portrays the variation of $N_{\rm t}$ on the concentration $\phi(\zeta)$. A higher $N_{\rm t}$ leads to a higher $\phi(\zeta)$. The concentration field $\phi(\zeta)$ versus the Schmidt number Sc is shown in Fig. 10. Clearly, $\phi(\zeta)$ decreases for a higher estimation of Sc. Physically, Sc defines a relationship between the momentum and mass diffusivity. A higher Schmidt number illustrates a smaller value of the mass diffusivity which yields a reduction in $\phi(\zeta)$. Figure 11 addresses the concentration field $\phi(\zeta)$ for the concentration slip parameter γ_3. By increasing γ_3, a weaker concentration field $\phi(\zeta)$ is observed. The roles of γ_1, λ, and F_r on the skin drag coefficients $f''(0)$ and $g'(0)$ are scrutinized in Figs. 12–15. It is recognized that the skin drag coefficients have an opposite trend for higher λ and F_r. Figures 16 and 17 depict that the local Nusselt number decreases with larger $N_{\rm t}$ and $N_{\rm b}$. Figures 18 and 19 illustrate the influence of $N_{\rm b}, N_{\rm t}$, and γ_3 on the mass transfer rate $-\phi(0)$. Clearly, the mass transfer rate enhances for higher estimations of $N_{\rm b}$ and γ_3.

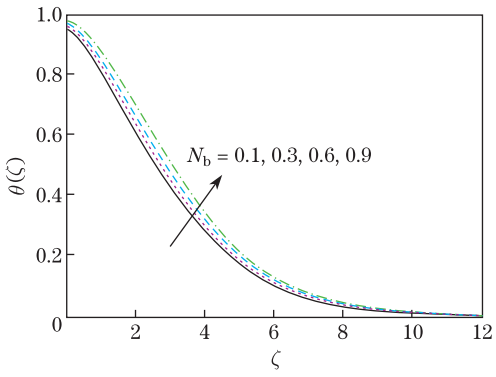

Fig. 2 Variations of temperature field $\theta(\zeta)$ against Brownian motion parameter $N_{\rm b}$, when $\lambda = 0.3$, $F_r = 0.2$, $\gamma_1 = 0.4$, $\gamma_2 = 0.6$, $\gamma_3 = 0.4$, $Ec = 0.7$, $Re_r = 1.0$, $Pr = Sc = 1.0$, and $N_{\rm t} = 0.2$ (color online)

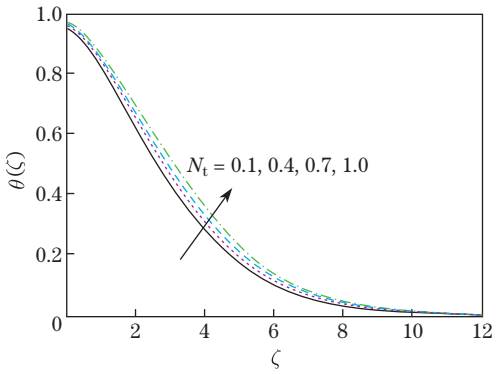

Fig. 3 Variations of temperature field $\theta(\zeta)$ against thermophoresis parameter $N_{\rm t}$, when $\lambda = 0.3$, $F_r = 0.2$, $\gamma_1 = 0.4$, $\gamma_2 = 0.6$, $\gamma_3 = 0.4$, $Ec = 0.7$, $Re_r = 1.0$, $Pr = Sc = 1.0$, and $N_{\rm b} = 0.3$ (color online)

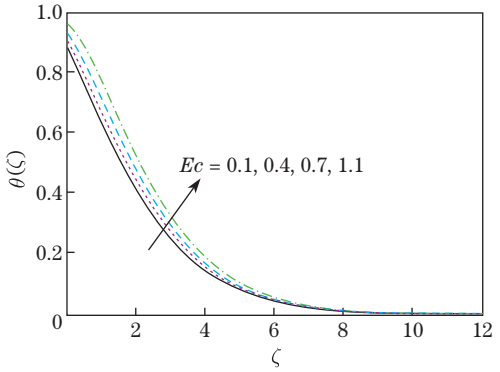

Fig. 4 Variations of temperature field $\theta(\zeta)$ against Eckert number Ec, when $\lambda = 0.3$, $F_r = 0.2$, $\gamma_1 = 0.4$, $\gamma_2 = 0.6$, $\gamma_3 = 0.4$, $Re_r = 1.0$, $Pr = Sc = 1.0$, $N_t = 0.2$, and $N_b = 0.3$ (color online)

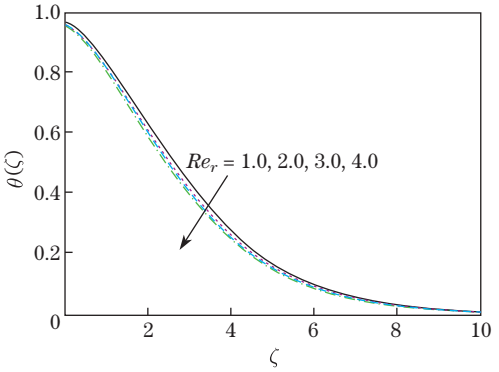

Fig. 5 Variations of temperature field $\theta(\zeta)$ against local Reynolds number Re_r, when $\lambda = 0.3$, $F_r = 0.2$, $\gamma_1 = 0.4$, $\gamma_2 = 0.6$, $\gamma_3 = 0.4$, $Ec = 0.7$, $Pr = Sc = 1.0$, $N_t = 0.2$, and $N_b = 0.3$ (color online)

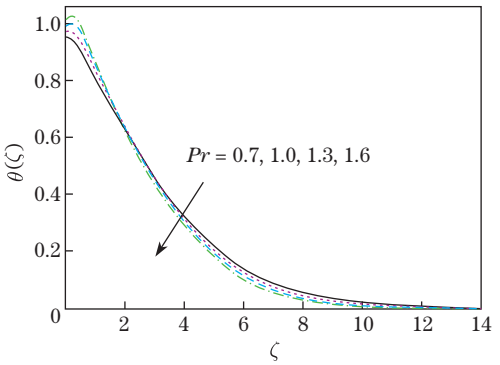

Fig. 6 Variations of temperature field $\theta(\zeta)$ against Prandtl number Pr, when $\lambda = 0.3$, $F_r = 0.2$, $\gamma_1 = 0.4$, $\gamma_2 = 0.6$, $\gamma_3 = 0.4$, $Ec = 0.7$, $Re_r = 1.0$, $Sc = 1.0$, $N_t = 0.2$, and $N_b = 0.3$ (color online)

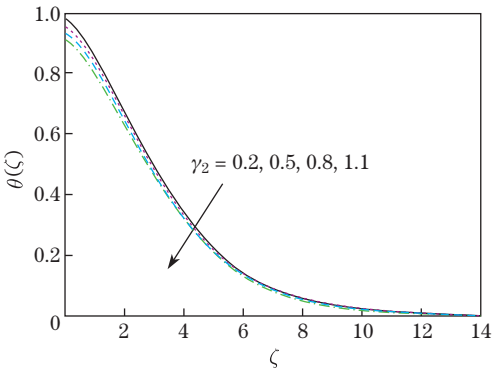

Fig. 7 Variations of temperature field $\theta(\zeta)$ against thermal slip parameter γ_2, when $\lambda = 0.3$, $F_r = 0.2$, $\gamma_1 = 0.4$, $\gamma_3 = 0.4$, $Re_r = 1.0$, $Ec = 0.7$, $Pr = Sc = 1.0$, $N_t = 0.2$, and $N_b = 0.3$ (color online)

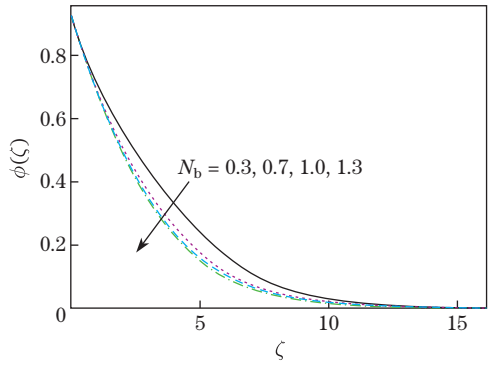

Fig. 8 Variations of concentration field $\phi(\zeta)$ against Brownian motion parameter N_b, when $\lambda = 0.3$, $F_r = 0.2$, $\gamma_1 = 0.4$, $\gamma_2 = 0.6$, $\gamma_3 = 0.4$, $Ec = 0.7$, $Re_r = 1.0$, $Pr = Sc = 1.0$, and $N_t = 0.2$ (color online)

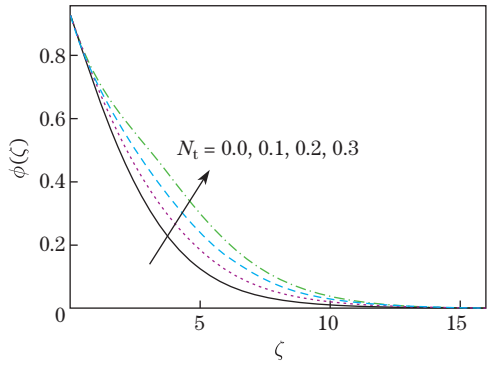

Fig. 9 Variations of concentration field $\phi(\zeta)$ against thermophoresis parameter N_t, when $\lambda = 0.3$, $F_r = 0.2$, $\gamma_1 = 0.4$, $\gamma_2 = 0.6$, $\gamma_3 = 0.4$, $Ec = 0.7$, $Re_r = 1.0$, $Pr = Sc = 1.0$, and $N_b = 0.3$ (color online)

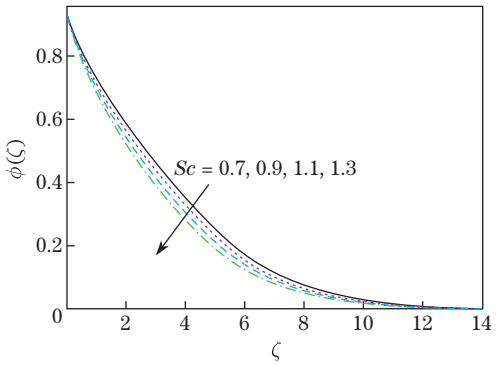

Fig. 10 Variations of concentration field $\phi(\zeta)$ against Schmidt number Sc, when $\lambda = 0.3$, $F_r = 0.2$, $\gamma_1 = 0.4$, $\gamma_2 = 0.6$, $\gamma_3 = 0.4$, $Ec = 0.7$, $Re_r = 1.0$, $Pr = 1.0$, $N_t = 0.2$, and $N_b = 0.3$ (color online)

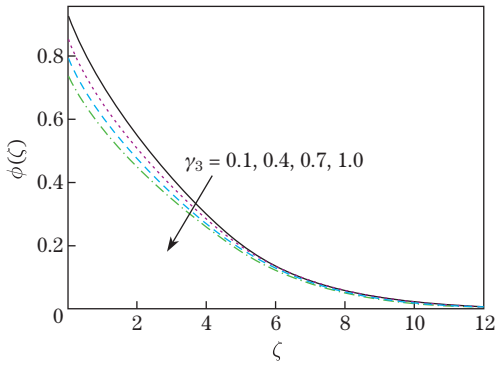

Fig. 11 Variations of concentration field $\phi(\zeta)$ against concentration slip parameter γ_3, when $\lambda = 0.3$, $F_r = 0.2$, $\gamma_1 = 0.4$, $\gamma_2 = 0.6$, $Ec = 0.7$, $Re_r = 1.0$, $Pr = Sc = 1.0$, $N_t = 0.2$, and $N_b = 0.3$ (color online)

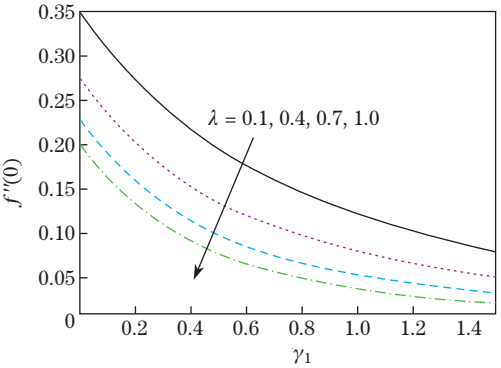

Fig. 12 Variations of skin friction coefficient $f''(0)$ against local porosity parameter λ and velocity slip parameter γ_1, when $F_r = 0.2$, $\gamma_2 = 0.6$, $\gamma_3 = 0.4$, $Re_r = 1.0$, $Ec = 0.7$, $Pr = Sc = 1.0$, $N_t = 0.2$, and $N_b = 0.3$ (color online)

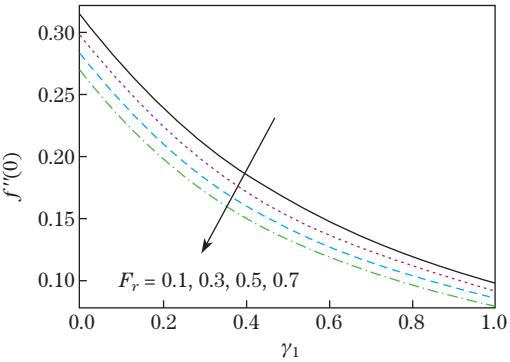

Fig. 13 Variations of skin friction coefficient $f''(0)$ against Forchheimer number F_r and velocity slip parameter γ_1, when $\lambda = 0.3$, $\gamma_2 = 0.5$, $\gamma_3 = 0.4$, $Re_r = 1.0$, $Ec = 0.7$, $Pr = Sc = 1.0$, $N_t = 0.2$, and $N_b = 0.3$ (color online)

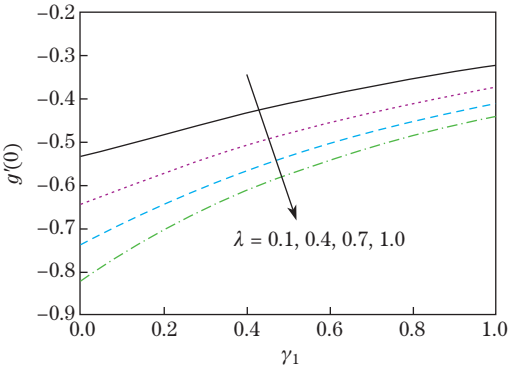

Fig. 14 Variations of skin friction coefficient $g'(0)$ against local porosity parameter λ and velocity slip parameter γ_1, when $F_r = 0.2$, $\gamma_2 = 0.6$, $\gamma_3 = 0.4$, $Re_r = 1.0$, $Ec = 0.7$, $Pr = Sc = 1.0$, $N_t = 0.2$, and $N_b = 0.3$ (color online)

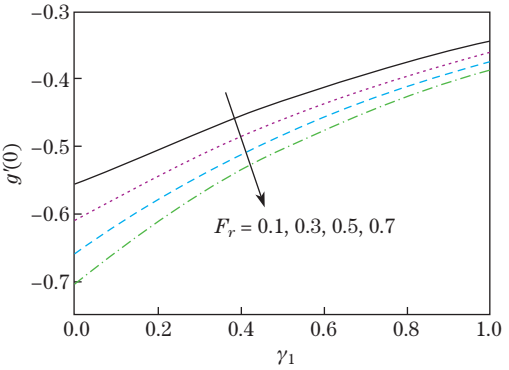

Fig. 15 Variations of skin friction coefficient $g'(0)$ against Forchheimer number F_r and velocity slip parameter γ_1, when $\lambda = 0.3$, $\gamma_2 = 0.6$, $\gamma_3 = 0.4$, $Re_r = 1.0$, $Ec = 0.7$, $Pr = Sc = 1.0$, $N_t = 0.2$, and $N_b = 0.3$ (color online)

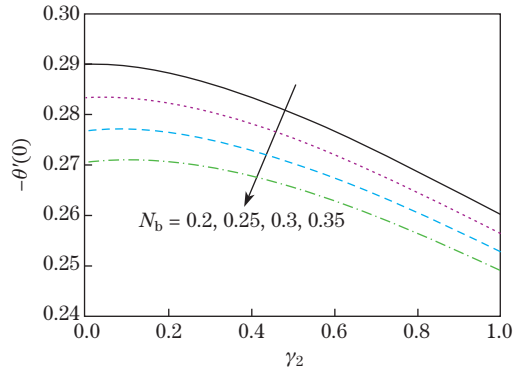

Fig. 16 Variations of local Nusselt number $-\theta'(0)$ against Brownian motion parameter N_b and thermal slip parameter γ_2, when $\lambda = 0.3$, $F_r = 0.2$, $\gamma_1 = 0.4$, $\gamma_3 = 0.4$, $Re_r = 1.0$, $Ec = 0.7$, $Pr = Sc = 1.0$, and $N_t = 0.2$ (color online)

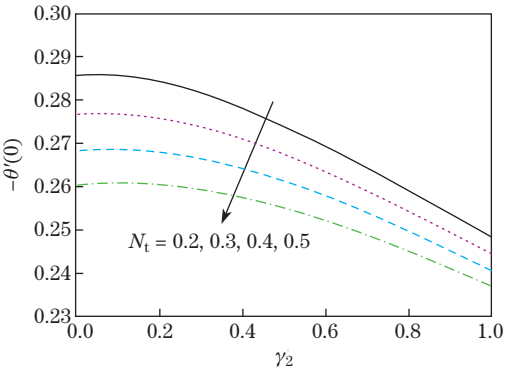

Fig. 17 Variations of local Nusselt number $-\theta'(0)$ against thermophoresis parameter N_t and thermal slip parameter γ_2, when $\lambda = 0.3$, $F_r = 0.2$, $\gamma_1 = 0.4$, $\gamma_3 = 0.4$, $Re_r = 1.0$, $Ec = 0.7$, $Pr = Sc = 1.0$, and $N_b = 0.3$ (color online)

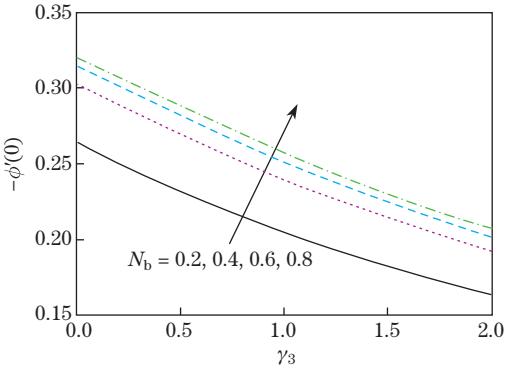

Fig. 18 Variations of local Sherwood number $-\phi'(0)$ against Brownian motion parameter N_b and concentration slip parameter γ_3, when $\lambda = 0.3$, $F_r = 0.2$, $\gamma_1 = 0.4$, $\gamma_2 = 0.6$, $Re_r = 0.9$, $Ec = 0.7$, $Pr = Sc = 1.0$, and $N_t = 0.2$ (color online)

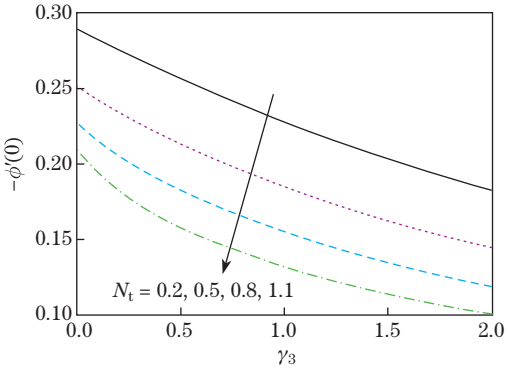

Fig. 19 Variations of local Sherwood number $-\phi'(0)$ against thermophoresis parameter N_t and concentration slip parameter γ_3, when $\lambda = 0.3$, $F_r = 0.2$, $\gamma_1 = 0.4$, $\gamma_2 = 0.6$, $Re_r = 1.0$, $Ec = 0.7$, $Pr = Sc = 1.0$, and $N_b = 0.3$ (color online)

6 Conclusions

The Darcy-Forchheimer flow of water-based nanofluids due to the rotation of a disk with partial slip conditions is examined. Main findings of current analysis are outlined below.

(i) The velocity field is reduced for a larger γ_1.

(ii) An improvement in the temperature is anticipated for higher N_b and N_t.

(iii) Both Re_r and Pr serve to reduce the temperature field.

(iv) As Sc enlarges, the concentration and the related layer thickness increase.

(v) The skin friction coefficient enhancement is observed for λ, F_r, and γ_3.

(vi) The local heat transfer rate prompts an increasing behavior for N_b and N_t.

References

[1] CHOI, S. U. S. Enhancing thermal conductivity of fluids with nanoparticles. *ASME International Mechanical Engineering Congress and Exposition*, **66**, 99–105 (1995)

[2] EASTMAN, J. A., CHOI, S. U. S., LI, S., YU, W., and THOMPSON, L. J. Anomalously increased effective thermal conductivities of ethylene glycol-based nanofluids containing copper nanoparticles. *Applied Physics Letters*, **78**, 718–720 (2001)

[3] BUONGIORNO, J. Convective transport in nanofluids. *ASME Journal of Heat Transfer*, **128**, 240–250 (2006)

[4] TIWARI, R. K. and DAS, M. K. Heat transfer augmentation in a two-sided lid-driven differentially heated square cavity utilizing nanofluid. *International Journal of Heat and Mass Transfer*, **50**, 2002–2018 (2007)

[5] ABU-NADA, E. and OZTOP, H. F. Effects of inclination angle on natural convection in enclosures filled with Cu-water nanofluid. *International Journal of Heat and Fluid Flow*, **30**, 669–678 (2009)

[6] HSIAO, K. L. Nanofluid flow with multimedia physical features for conjugate mixed convection and radiation. *Computers and Fluids*, **104**, 1–8 (2014)

[7] HSIAO, K. L. Stagnation electrical MHD nanofluid mixed convection with slip boundary on a stretching sheet. *Applied Thermal Engineering*, **98**, 850–861 (2016)

[8] SHEHZAD, N., ZEESHAN, A., ELLAHI, R., and VAFAI, K. Convective heat transfer of nanofluid in a wavy channel: Buongiorno's mathematical model. *Journal of Molecular Liquids*, **222**, 446–455 (2016)

[9] MAHANTHESH, B., MABOOD, F., GIREESHA, B. J., and GORLA, R. S. R. Effects of chemical reaction and partial slip on the three-dimensional flow of a nanofluid impinging on an exponentially stretching surface. *European Physical Journal Plus*, **132**, 113 (2017)

[10] FAROOQ, M., JAVED, M., KHAN, M. I., ANJUM, A., and HAYAT, T. Melting heat transfer and double stratification in stagnation flow of viscous nanofluid. *Results in Physics*, **7**, 2296–2301 (2017)

[11] KUMAR, K. G., RAMESH, G. K., GIREESHA, B. J., and GORLA, R. S. R. Characteristics of Joule heating and viscous dissipation on three-dimensional flow of Oldroyd B nanofluid with thermal radiation. *Alexandria Engineering Journal*, **57**, 2139–2149 (2018)

[12] HAYAT, T., RASHID, M., ALSAEDI, A., and AHMAD, B. Flow of nanofluid by nonlinear stretching velocity. *Results in Physics*, **8**, 1104–1109 (2018)

[13] USMAN, M., SOOMRO, F. A., HAQ, R. U., WANG, W., and DEFTERLI, O. Thermal and velocity slip effects on Casson nanofluid flow over an inclined permeable stretching cylinder via collocation method. *International Journal of Heat and Mass Transfer*, **122**, 1255–1263 (2018)

[14] IMTIAZ, M., SHAHID, F., HAYAT, T., and ALSAEDI, A. Melting heat transfer in Cu-water and Ag-water nanofluids flow with homogeneous-heterogeneous reactions. *Applied Mathematics and Mechanics* (*English Edition*), **40**(4), 465–480 (2019) https://doi.org/10.1007/s10483-019-2462-8

[15] PRAKASH, J., TRIPATHI, D., TIWARI, A. K., SAIT, S. M., and ELLAHI, R. Peristaltic pumping of nanofluids through tapered channel in porous environment: applications in blood flow. *Symmetry*, **11**, 868 (2019)

[16] SARAFRAZ, M. M., POURMEHRANA, O., YANGA, B., ARJOMANDIA, M., and ELLAHI, R. Pool boiling heat transfer characteristics of iron oxide nano-suspension under constant magnetic field. *International Journal of Thermal Sciences*, **147**, 106131 (2020)

[17] NIAZI, M. D. K. and XU, H. Modelling two-layer nanofluid flow in a micro-channel with electro-osmotic effects by means of Buongiorno's model. *Applied Mathematics and Mechanics* (*English Edition*), **41**(1), 83–104 (2020) https://doi.org/10.1007/s10483-020-2558-7

[18] FORCHHEIMER, P. Wasserbewegung durch boden. *Zeitschrift des Vereins Deutscher Ingenieure*, **45**, 1781–1788 (1901)

[19] MUSKAT, M. *The Flow of Homogeneous Fluids Through Porous Media*, Edwards, MI (1946)

[20] SEDDEEK, M. A. Influence of viscous dissipation and thermophoresis on Darcy-Forchheimer mixed convection in a fluid saturated porous media. *Journal of Colloid and Interface Science*, **293**, 137–142 (2006)

[21] SADIQ, M. A. and HAYAT, T. Darcy-Forchheimer flow of magneto Maxwell liquid bounded by convectively heated sheet. *Results in Physics*, **6**, 884–890 (2016)

[22] BAKAR, S. A., ARIFIN, N. M., NAZAR, R., ALI, F. M., and POP, I. Forced convection boundary layer stagnation-point flow in Darcy-Forchheimer porous medium past a shrinking sheet. *Frontiers in Heat and Mass Transfer*, **7**, 38 (2016)

[23] UMAVATHI, J. C., OJJELA, O., and VAJRAVELU, K. Numerical analysis of natural convective flow and heat transfer of nanofluids in a vertical rectangular duct using Darcy-Forchheimer-Brinkman model. *International Journal of Thermal Sciences*, **111**, 511–524 (2017)

[24] HAYAT, T., NAZAR, H., IMTIAZ, M., and ALSAEDI, A. Darcy-Forchheimer flows of copper and silver water nanofluids between two rotating stretchable disks. *Applied Mathematics and Mechanics* (*English Edition*), **38**(12), 1663–1678 (2017) https://doi.org/10.1007/s10483-017-2289-8

[25] HAYAT, T., AZIZ, A., MUHAMMAD, T., and ALSAEDI, A. An optimal analysis for Darcy-Forchheimer 3D flow of nanofluid with convective condition and homogeneous-heterogeneous reactions. *Physics Letterrs A*, **382**, 2846–2855 (2018)

[26] HAYAT, T., HAIDER, F., MUHAMMAD, T., and ALSAEDI, A. Darcy-Forchheimer squeezed flow of carbon nanotubes with thermal radiation. *Journal of Physics and Chemistry of Solids*, **120**, 79–86 (2018)

[27] ULLAH, M. Z., ALSHOMRANI, A. S., and ALGHAMDI, M. Significance of Arrhenius activation energy in Darcy-Forchheimer 3D rotating flow of nanofluid with radiative heat transfer. *Physica A*: *Statistical Mechanics and Its Applications*, 124024 (2019) https://doi.org/10.1016/j.physa.2019.124024

[28] FANG, T. G. and WANG, F. J. Momentum and heat transfer of a special case of the unsteady stagnation-point flow. *Applied Mathematics and Mechanics* (*English Edition*), **41**(1), 51–82 (2020) https://doi.org/10.1007/s10483-020-2556-9

[29] SAIF, R. S., MUHAMMAD, T., and SADIA, H. Significance of inclined magnetic field in Darcy-Forchheimer flow with variable porosity and thermal conductivity. *Physica A*: *Statistical Mechanics and Its Applications*, 124067 (2020) https://doi.org/10.1016/j.physa.2019.124067

[30] VON KÁRMÁN, T. V. Über laminare and turbulente reibung. *Zeitschrift für Angewandte Mathematik und Mechanik*, **1**, 233–252 (1921)

[31] TURKYILMAZOGLU, M. and SENEL, P. Heat and mass transfer of the flow due to a rotating rough and porous disk. *International Journal of Thermal Sciences*, **63**, 146–158 (2013)

[32] RASHIDI, M. M., KAVYANI, N., and ABELMAN, S. Investigation of entropy generation in MHD and slip flow over rotating porous disk with variable properties. *International Journal of Heat and Mass Transfer*, **70**, 892–917 (2014)

[33] TURKYILMAZOGLU, M. Nanofluid flow and heat transfer due to a rotating disk. *Computers and Fluids*, **94**, 139–146 (2014)

[34] HATAMI, M., SHEIKHOLESLAMI, M., and GANJI, D. D. Laminar flow and heat transfer of nanofluids between contracting and rotating disks by least square method. *Powder Technology*, **253**, 769–779 (2014)

[35] MUSTAFA, M., KHAN, J. A., HAYAT, T., and ALSAEDI, A. On Bödewadt flow and heat transfer of nanofluids over a stretching stationary disk. *Journal of Molecular Liquids*, **211**, 119–125 (2015)

[36] SHEIKHOLESLAMI, M., HATAMI, M., and GANJI, D. D. Numerical investigation of nanofluid spraying on an inclined rotating disk for cooling process. *Journal of Molecular Liquids*, **211**, 577–583 (2015)

[37] DOH, D. H. and MUTHTAMILSELVAN, M. Thermophoretic particle deposition on magnetohydrodynamic flow of micropolar fluid due to a rotating disk. *International Journal of Mechanical Sciences*, **130**, 350–359 (2017)

[38] QAYYUM, S., IMTIAZ, M., ALSAEDI, A., and HAYAT, T. Analysis of radiation in a suspension of nanoparticles and gyrotactic microorganism for rotating disk of variable thickness. *Chinese Journal of Physics*, **56**, 2404–2423 (2018)

[39] XU, H. Modelling unsteady mixed convection of a nanofluid suspended with multiple kinds of nanoparticles between two rotating disks by generalized hybrid model. *International Communications in Heat and Mass Transfer*, **108**, 104275 (2019)

[40] MAJEED, A. H., BILAL, S., MAHMOOD, R., and MALIK, M. Y. Heat transfer analysis of viscous fluid flow between two coaxially rotated disks embedded in permeable media by capitalizing non-Fourier heat flux model. *Phyisca A*: *Statistical Mechanics and Its Applications*, **540**, 123182 (2020)

[41] LIAO, S. J. An optimal homotopy-analysis approach for strongly nonlinear differential equations. *Communications in Nonlinear Science and Numerical Simulation*, **15**, 2003–2016 (2010)

[42] MALVANDI, A., HEDAYATI, F., and DOMAIRRY, G. Stagnation point flow of a nanofluid toward an exponentially stretching sheet with nonuniform heat generation/absorption. *Journal of Thermodynamics*, **2013**, 764827 (2013)

[43] ABBASBANDY, S., HAYAT, T., ALSAEDI, A., and RASHIDI, M. M. Numerical and analytical solutions for Falkner-Skan flow of MHD Oldroyd-B fluid. *International Journal of Numerical Methods for Heat and Fluid Flow*, **24**, 390–401 (2014)

[44] TURKYILMAZOGLU, M. An effective approach for evaluation of the optimal convergence control parameter in the homotopy analysis method. *Filomat*, **30**, 1633–1650 (2016)

[45] AWAIS, M., SALEEM, S., HAYAT, T., and IRUM, S. Hydromagnetic couple-stress nanofluid flow over a moving convective wall: OHAM analysis. *Acta Astronautica*, **129**, 271–276 (2016)

[46] HAQ, R. U., HAMOUCH, Z., HUSSAIN, S. T., and MEKKAOUI, T. MHD mixed convection flow along a vertically heated sheet. *International Journal of Hydrogen Energy*, **42**, 15925–15932 (2017)

[47] AWAIS, M., AWAN, S. E., IQBAL, K., KHAN, Z. A., and RAJA, M. A. Z. Hydromagnetic mixed convective flow over a wall with variable thickness and Cattaneo-Christov heat flux model: OHAM analysis. *Results in Physics*, **8**, 621–627 (2018)

[48] GUPTA, S., KUMAR, D., and SINGH, J. MHD mixed convective stagnation point flow and heat transfer of an incompressible nanofluid over an inclined stretching sheet with chemical reaction and radiation. *International Journal of Heat and Mass Transfer*, **118**, 378–387 (2018)

[49] ULLAH, I., RAHIM, M. T., KHAN, H., and QAYYUM, M. Analysis of various semi-numerical schemes for magnetohydrodynamic (MHD) squeezing fluid flow in porous medium. *Propulsion and Power Research*, **8**, 69–78 (2019)

[50] NAZ, R., TARIQ, S., and ALSULAMI, H. Inquiry of entropy generation in stratified Walters' B nanofluid with swimming gyrotactic microorganisms. *Alexandria Engineering Journal*, **59**, 247–261 (2020)